Medium Access Control and Rate Adaptation for Ultrasonic Intrabody Sensor Networks

G. Enrico Santagati, *Student Member, IEEE*, Tommaso Melodia, *Member, IEEE*, Laura Galluccio, *Member, IEEE*, and Sergio Palazzo, *Senior Member, IEEE*

***Abstract*—The use of wirelessly internetworked miniaturized biomedical devices is promising a significant leap forward in medical treatment of many pervasive diseases. Recognizing the limitations of traditional radio-frequency wireless communications in interconnecting devices within the human body, in this paper, we propose for the first time to develop network protocols for implantable devices based on ultrasonic transmissions. We start off by assessing the theoretical feasibility of using ultrasonic waves in human tissues and by deriving an accurate channel model for ultrasonic intrabody communications. Then, we propose a new ultrasonic transmission and multiple access technique, which we refer to as *Ultrasonic WideBand* (UsWB). UsWB is based on the idea of transmitting information bits spread over very short pulses following a time-hopping pattern. The short impulse duration results in limited reflection and scattering effects, and the low duty cycle reduces the impact of thermal and mechanical effects, which may be detrimental for human health. We then develop a multiple access technique with distributed control to enable efficient simultaneous access by mutually interfering devices based on minimal and localized information exchange and on measurements at the receiver only. Finally, we demonstrate the performance of UsWB through a multiscale simulator that models the proposed communication system at the acoustic wave level, at the physical (bit) level, and at the network (packet) level. We also validate the simulation results by comparing them to experimental results obtained with a software-defined testbed.**

***Index Terms*—Acoustic communications, body area networks, medium access control, sensor networks, ultrasonic networking.**

I. Introduction

BODY area networks have received considerable attention in the last few years [2], driven by the fascinating promise of a future where carefully engineered miniaturized biomedical devices implanted, ingested, or worn by humans are wirelessly internetworked to collect diagnostic information and to fine-tune medical treatments over extended periods of time [3], [4]. Potential applications include measuring the level of glucose in the blood of diabetic patients and reactively controlling the administration of insulin through under-skin actuators, monitoring the digestive tract through pill-sized ingestible cameras, or monitoring bone growth for diabetes treatment. Furthermore, these technologies may enhance minimally intrusive microsurgery, thus overcoming the limitations of currently available catheter technology.

Yet, most research to date has focused on communications *along the body surface* among devices that use traditional electromagnetic radio frequency (RF) carrier waves, while the underlying challenge of enabling networked *intrabody* miniaturized (at the micro or nano scale) sensors and actuators that communicate through body tissues is substantially unaddressed. The main obstacle to enabling this vision of networked implantable devices is posed by the physical nature of propagation in the human body, which is composed primarily (65%) of water, a medium through which RF electromagnetic waves do not propagate well, even at relatively low frequencies. For this reason, much research in this area has focused on reducing the radiated power to avoid overheating of tissues [5].

These formidable challenges cannot be overcome unless a major paradigm shift in networking through body tissues is made to address the limitations of RF propagation in the human body. Therefore, in this paper, *we propose the use of ultrasonic waves to wirelessly internetwork intrabody devices.*

Acoustic waves, typically generated through piezoelectric materials, are known to propagate better than their RF counterpart in media composed mainly of water. Since World War II, piezoelectrically generated acoustic waves have found application, among others, in underwater communications (typically at frequencies between 0 and 100 kHz [6]), in indoor localization in sensor networks [7], and, massively, in ultrasonic medical imaging [8], [9]. While communication at low frequencies requires sizable transducers, innovations in piezoelectric materials and fabrication methods, primarily driven by the need for resolution in medical imaging, have made miniaturized transducers, at the micro [10], [11] and even nano scales [12] a reality. Moreover, the medical experience of the last decades has demonstrated that ultrasounds are fundamentally safe, as long as acoustic power dissipation in tissues is limited to predefined safety levels [3], [4], [13]. It is also known that ultrasonic heat dissipation in tissues is minimal compared to RF waves [14].

In this paper, we lay our foundation on the fundamental physics of ultrasound propagation and move up layers of the protocol stack with the following core contributions.

Manuscript received May 22, 2013; revised November 23, 2013 and February 05, 2014; accepted April 03, 2014; approved by IEEE/ACM TRANSACTIONS ON NETWORKING Editor Y. Liu. Date of publication April 29, 2014; date of current version August 14, 2015. This work is based on material supported in part by the US National Science Foundation under Grant CNS-1253309. A preliminary shorter version of this paper appeared in the Proceedings of the IEEE International Conference on Sensor, Mesh and Ad Hoc Communications and Networks (SECON), New Orleans, LA, USA, June 24–27, 2013.

G. E. Santagati and T. Melodia are with the Department of Electrical Engineering, University at Buffalo, The State University of New York, Buffalo, NY 14260 USA (e-mail: santagat@buffalo.edu; tmelodia@buffalo.edu).

L. Galluccio and S. Palazzo are with the Dipartimento di Ingegneria Elettrica, Elettronica ed Informatica, University of Catania, 95127 Catania, Italy (e-mail: laura.galluccio@dieei.unict.it; sergio.palazzo@dieei.unict.it).

Color versions of one or more of the figures in this paper are available online at http://ieeexplore.ieee.org.

Digital Object Identifier 10.1109/TNET.2014.2316675

- *Feasibility of ultrasonic communications in the human body.* We start off by assessing the feasibility of using ultrasounds for intrabody communications. We discuss fundamental aspects of ultrasonic propagation in tissues and explore important tradeoffs, including the choice of a transmission frequency, transmission power, bandwidth, and transducer size.
- *Ultrasonic channel modeling.* We then proceed to derive a channel model for ultrasonic communications in the human body. We focus on propagation of ultrasounds at the wave level to obtain a model of the channel impulse response. We find that the inhomogeneity of the human body, characterized by a multitude of small organs and tissues, causes severe multipath effect. We observe that reflectors and scatterers cause numerous delayed versions of the transmitted signal to reach the receiver, thus making detection and decoding a challenging operation. In addition, we observe that the low speed of sound in tissues leads to high delays that need to be considered in system design.
- *Ultrasonic wideband design.* To address the severe effect of multipath, we design and propose a new transmission and multiple access technique, which we refer to as Ultrasonic WideBand (UsWB). Ultrasonic wideband is based on the idea of transmitting very short pulses following an adaptive time-hopping pattern. The short impulse duration results in limited reflection and scattering effects, and the low duty cycle reduces thermal and mechanical effects that are detrimental for human health. A variable-length spreading code is superimposed to the time-hopping pattern to further combat the effect of multipath and to introduce waveform diversity among interfering nodes.
- *Ultrasonic wideband adaptation and multiple access control*. We study and develop medium access techniques with distributed control to enable multiple access among interfering implanted devices. The proposed scheme is based on the idea of regulating the data rate of each transmitter to adapt to the current level of interference by distributively optimizing the code length and duration of the time-hopping frame. We show how the proposed distributed algorithm is effective in adapting the network throughput to the current level of interference based on minimal and localized information exchange.
- *System performance evaluation.* We evaluate the proposed scheme through a multiscale simulator that evaluates our system at three different levels, i.e.: 1) at the wave level by modeling ultrasonic propagation through reflectors and scatterers; 2) at the bit level by simulating in detail the proposed ultrasonic transmission scheme; 3) at the packet level by simulating networked operations and distributed control and adaptation to evaluate metrics such as network throughput and packet drop rate. We also validate simulation results through experiments obtained through a software-defined ultrasonic testbed.

The rest of the paper is organized as follows. In Sections II and III, we discuss fundamental aspects of ultrasonic physical propagation in human tissues and channel modeling. In Section IV, we outline the design of UsWB, and in Section V we illustrate the proposed medium access control protocol. Performance evaluation results are discussed in Section VI along with tested validation of the simulation results. Finally, in Section VII we discuss related work, and in Section VIII we conclude the paper.

II. Ultrasonic Propagation in Human Tissues

Ultrasonic waves originate from the propagation of mechanical vibrations of particles in an elastic medium at frequencies above the upper limit for human hearing, i.e., 20 kHz. Acoustic propagation through a medium is governed by the acoustic wave equation (referred to as the Helmhotz equation), which describes pressure variation over the three dimensions

$$\nabla^2 P - \frac{1}{c^2}\frac{\partial^2 P}{\partial t^2} = 0 \tag{1}$$

where $P(x, y, z, t)$ represents the acoustic pressure scalar field in space and time, and c is the propagation speed in the medium. The Helmholtz equation can be derived from the continuity equation, the force equation, and the equation of state [15].

When ultrasonic waves propagate through an absorbing medium, the initial pressure P_0 reduces to $P(d)$ at a distance d [16] as

$$P(d) = P_0 e^{-\alpha d} \tag{2}$$

where α ($[\mathrm{Np} \cdot \mathrm{cm}^{-1}]$) is the amplitude attenuation coefficient that captures energy dissipation from the ultrasonic beam and is a function of the carrier frequency f as $\alpha = af^b$ [16], where a ($[\mathrm{Np} \cdot \mathrm{m}^{-1}\,\mathrm{MHz}^{-b}]$) and b are tissue attenuation parameters.

In [3], we observed that the attenuation level in tissues can be significant, and it increases with the distance between transmitter and receiver. Moreover, as discussed in [17], the beam spread is inversely proportional to the ratio between the diameter of the radiating surface and the wavelength corresponding to the operating frequency [3]. Consequently, since most biomedical sensing applications require directional transducers, one needs to operate at high frequencies to keep the transducer size small. However, as expected, higher frequencies lead to higher attenuation.

In Fig. 1, we show the maximum "allowed" carrier frequency with respect to distance, for different values of the maximum tolerable attenuation. We consider blood as the propagation medium and limit the maximum operating frequency to 1 GHz. In Table I, we summarize our findings [3] on the maximum "allowed" carrier frequency for a 100-dB maximum tolerable attenuation. For distances ranging between some micrometers up to a few millimeters (i.e., short-range communications), frequencies higher than 1 GHz can be used. When distances are higher than 1 mm but still lower than some centimeters, i.e., for medium-range communications, the transmission frequency should be decreased to approximately 100 MHz. For distances higher than a few centimeters, i.e., for long-range communications, the transmission frequency should not exceed 10 MHz. Similar results in [3] are independently reported in [4].

III. Channel Modeling

The first step toward the design of high-performance ultrasonic intrabody networks is to characterize the communication

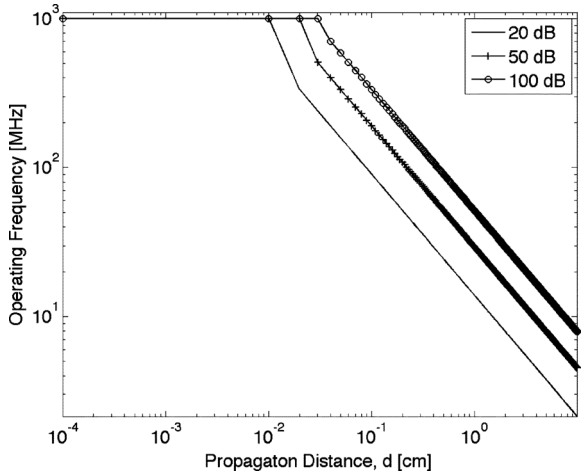

Fig. 1. Operating frequency as a function of the propagation distance, with different values of the tolerable attenuation.

TABLE I
FREQUENCY LIMITS FOR $A = 100$ dB

Communication Range	Distance	Frequency Limit
Short Range	μm - mm	$> 1GHz$
Medium Range	mm - cm	$\simeq 100MHz$
Long Range	>cm	$\simeq 10MHz$

channel in tissues—for which, unfortunately, there is no literature available to date, except for [18] where the authors present a simple two-dimensional statistical model. Here, we derive a deterministic channel model based on acoustic wave propagation theory.

Propagation of acoustic waves through biological tissues is governed by three coupled first-order equations, i.e., the *continuity equation*, the *force equation*, and the *equation of state* [15], which represent relationships among acoustic pressure P, acoustic particle velocity u, and medium density ρ, and can be rearranged to obtain the Helmholtz equation in Section II. A realistic model of ultrasonic propagation in human tissues that incorporates attenuation, scattering, and multipath effect needs to satisfy the three above equations simultaneously.

Traditionally, partial differential equations are solved using numerical methods such as the finite-difference method (FDM). We take a different, computationally more efficient approach, based on the pseudo-spectra (PS)l and k-space methods [19]. Basically, the PS method reduces the computational complexity in the spatial domain by using Fourier series expansions and fast Fourier transforms (FFTs), while the k-space method operates in the time domain by using k-space propagator functions (instead of classical finite differences) to approximate temporal derivatives. As a consequence, larger time-steps can be used, reducing the simulation time with controllable accuracy. k-Wave [20] is a powerful tool implementing this method.

We modeled a reference ultrasonic propagation channel in the human body to derive an accurate characterization of the channel impulse response, which was then used in PHY- and medium access control (MAC)-layer simulation studies. Specifically, we first modeled a section of the human arm, including bones, muscles, fat, and skin. We considered a heterogeneous

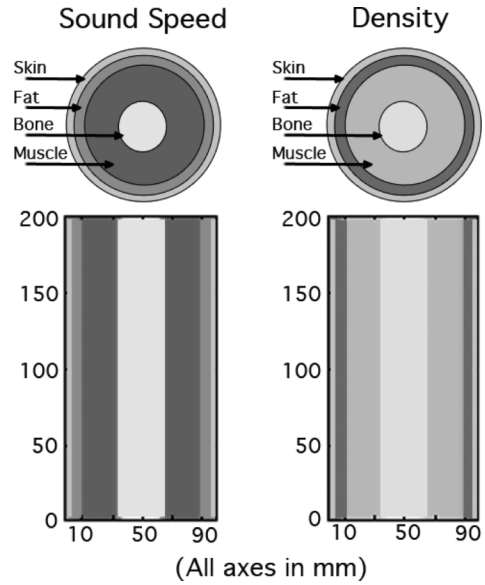

Fig. 2. Sound speed and density distributions in the modeled human arm.

TABLE II
TISSUES PARAMETERS

Tissue	c [m/s]	ρ [Kg/m^3]	a [Np $\cdot$ cm^{-1}MHz^{-b}]
Bone	2407	1920	1.8
Muscle	1629	1056	0.125
Fat	1487	939	0.093
Skin	1729	1190	0.212

two-dimensional rectangular area of length 20 cm and width 10 cm, where density and sound velocity are distributed as shown in Fig. 2. The bone half-section is 18 mm wide, the muscle half-section is 22 mm wide, while fat and skin have a half-section 7 and 3 mm wide, respectively. The medium parameters sound speed c, density ρ, and attenuation a are reported in Table II [21]. The attenuation parameter b is set to 1 for all considered tissues.

We obtained the channel impulse response by releasing an omnidirectional ideal Dirac pulse in the left top corner of the muscle section. The receiver is located at the left bottom corner of the muscle section. Transmitter and receiver are located 20 cm away from one another. In Fig. 3, we show snapshots of the acoustic field time propagation in the modeled environment. We observe that the effect of the bone and tissues is to partially reflect and scatter the acoustic wave transmitted by the source. We then obtain the channel impulse response by recording the time series of the signal at the receiver sensor.

Fig. 4 (top) reports the resulting impulse response in this scenario. We observe that multipath and scattering effects introduce attenuated signal replicas spaced in time. Because of the very short duration of the transmitted pulses, replicas do not interact destructively, which provides a strong motivation for the transmission scheme proposed in Section IV. Based on this, we can model the channel response as a complex-valued low-pass equivalent impulse response, as $h(\tau,t) = \sum_{k=1}^{K} a_k(t)\delta(\tau - \tau_k)e^{j\theta_k(t)}$, where δ is the Dirac delta function, K is the number of resolvable multipath components, τ_k is the delay of the multipath components, a_k is the path amplitude value, and θ_k is the path phase value. With this description, we can characterize

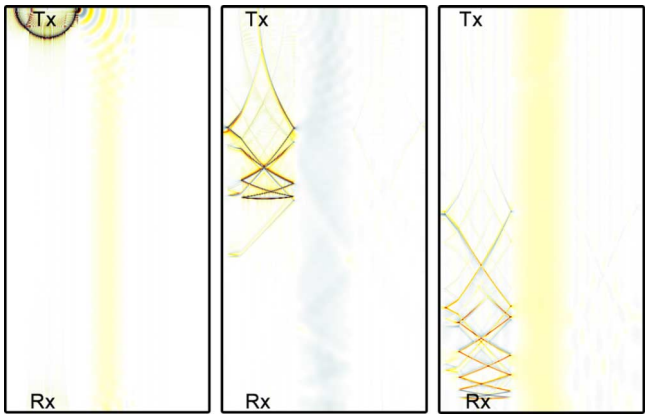

Fig. 3. Snapshots of the time evolution of the acoustic field in the modeled human arm.

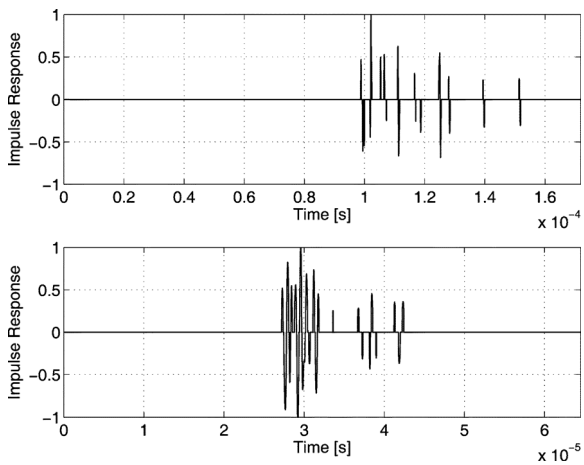

Fig. 4. Resulting ultrasonic normalized channel impulse response in *(top)* the modeled 2-D human arm and *(bottom)* 3-D human kidney.

the channel through the mean excess delay (τ_{m}) and the RMS delay spread (τ_{RMS}). For the channel simulated above, we obtained $\tau_{\mathrm{m}} = 4.4353 \cdot 10^{-6}$ s and $\tau_{\mathrm{RMS}} = 2.3389 \cdot 10^{-6}$ s. Since the coherence bandwidth of the channel is proportional to the inverse of τ_{RMS}, we should consider this channel as frequency-selective for signals of bandwidth above approximately 85 kHz [22].

We also modeled a three-dimensional human kidney enclosed in a background medium with similar density and speed of sound. This model accurately reproduces the characteristics of a commercial ultrasonic phantom that mimics the propagation characteristic of human kidney [23]. The background medium has very low attenuation coefficient, i.e., it is almost transparent to ultrasonic propagation. The medium parameters of sound speed c, density ρ, and attenuation a are as in Table III. In Fig. 5, we show the density distribution in the three section planes, with each plane crossing the kidney in the middle. We repeated similar simulations considering a three-dimensional setup and assuming that the pulse transmitter is located at the top side of the kidney in the xy-plane and in the middle of the xz- and yz-planes. In Fig. 4 (bottom), we show the result of the three-dimensional pulse propagation. We observe that since the medium is more homogeneous than in the previous case

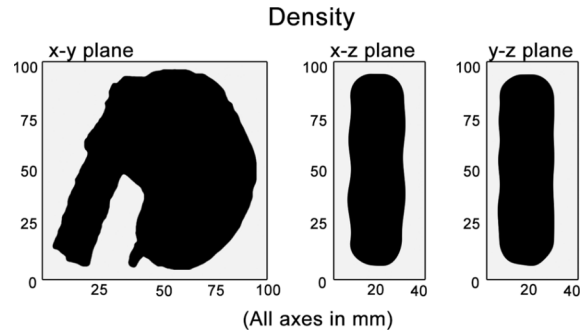

Fig. 5. Density distributions in the modeled human kidney.

TABLE III
TISSUE PARAMETERS

Tissue	c [m/s]	ρ [Kg/m^3]	a [Np $\cdot$ cm^{-1}MHz$^{-\mathrm{b}}$]
Kidney	1550	1030	0.046
Background Gel	1550	1020	0.011

because of the absence of bones, the channel impulse response shows a reduced number of pulse replicas and a more regular attenuation pattern. By characterizing the channel response as a complex-valued low-pass equivalent impulse response, we obtain $\tau_{\mathrm{m}} = 8.8256 \cdot 10^{-7}$ s and $\tau_{\mathrm{RMS}} = 1.3924 \cdot 10^{-6}$ s. The coherence bandwidth of the channel is in this case 140 kHz.

IV. ULTRASONIC WIDEBAND

Based on the considerations summarized in Sections II and III, we design and propose a new ultrasonic transmission and multiple access technique, which we refer to as UsWB. The key design objectives of UsWB are the following:

- to enable low-complexity and reliable communications in ultrasonic channels against the effect of multipath reflections within the human body;
- to limit the thermal effect of communications, which is detrimental to human health;
- to enable distributed medium access control and rate adaptation to combat the effect of interference from co-located and simultaneously transmitting devices.

UsWB is jointly designed to provide physical-layer functionalities and medium access control arbitration and adaptation to enable multiple concurrent co-located transmissions with minimal coordination.

Ultrasonic Pulsed Transmissions: Ultrasonic wideband is based on the idea of transmitting very short ultrasonic pulses following an *adaptive* time-hopping pattern together with a superimposed adaptive spreading code. Baseband pulsed transmissions enable high data rate, low-power communications, and low-cost transceivers and have been proposed for RF short-range, high-data-rate communications [24], [25], although with much shorter pulse durations (and consequently larger bandwidth) than achievable in ultrasonic communications.

The characteristics of pulsed transmissions appear to ideally address all the requirements discussed above. Their fine delay-resolution properties are well suited for propagation in the human body, where inhomogeneity in terms of density

and propagation speed, as well as the pervasive presence of very small organs and particles, cause dense multipath and scattering. When replicas of pulses reflected or scattered are received with a differential delay at least equal to the pulse width, they do not overlap in time with the original pulse. Therefore, for pulse durations in the order of hundreds of nanoseconds [10], pulse overlaps in time are reduced, and multiple propagation paths can be efficiently resolved and combined at the receiver to reduce the bit error rate (BER). Also, the low duty cycle of pulsed transmissions reduces the impact of thermal and mechanical effects, which are detrimental for human health [26]. Observe also that the large instantaneous bandwidth enables fine time resolution for accurate position estimation [6] and network synchronization. Finally, carefully designed interference mitigation techniques may enable MAC protocols that do not require mutual temporal exclusion between different transmitters. This is crucial in the ultrasonic transmission medium since the propagation speed is about 1500 m/s and consequently the propagation delay is five orders of magnitude higher than in RF in-air channels (where the propagation speed is about $3 \cdot 10^8$ m/s) and carrier-sense-based medium access control protocols are ineffective [6]. In addition, data rate can be flexibly traded for power spectral density and multipath performance.

A. Physical Layer Model

Adaptive Time-Hopping: Consider a slotted time divided in chips of duration $T_{\rm c}$, with chips organized in frames of duration $T_{\rm f} = N_{\rm h} \cdot T_{\rm c}$, where $N_{\rm h}$ is the number of chips per frame. Each user transmits one pulse in one chip per frame and determines in which chip to transmit based on a pseudorandom *time-hopping sequence* (THS), i.e., a sequence generated by seeding a random number generator with the user's unique ID.

The train of pulses is modulated based on pulse position modulation (PPM), i.e., a "1" symbol is carried by a pulse delayed by a time δ with respect to the beginning of the chip, while a "0" symbol begins with the chip. The signal $s^{(k)}(t,i)$ generated by the kth user to convey the ith symbol is expressed as

$$s^{(k)}(t,i) = p(t - c_i^{(k)} T_{\rm c} - iT_{\rm f} - d_i^{(k)}\delta) \tag{3}$$

where $p(t)$ is the second derivative of a Gaussian Pulse, $\{c_i^{(k)}\}$ is the time-hopping sequence of the kth source, with $0 \le c_i^{(k)} \le N_{\rm h} - 1$, and $\{d_i^{(k)}\}$ is the information-bearing sequence, $d_i^{(k)} \in \{0,1\}$. The resulting data rate, in pulses per second, is expressed as

$$R(N_{\rm h}) = \frac{1}{T_{\rm f}} = \frac{1}{N_{\rm h} T_{\rm c}}. \tag{4}$$

By regulating the time-hopping frame length $N_{\rm h}$, i.e., the average interpulse time, a user can adapt its transmission rate, and as a consequence modify the average radiated power and therefore the level of interference generated to other ongoing communications. We observe that an individual user has little incentive to increase its frame size since that results in a lower achievable data rate, without any major benefit for the user itself (since the level of interference perceived depends primarily on the frame length of the other users, and not on its own). However, a longer time frame reduces the interference generated to the other users. Therefore, selfish/greedy frame adaptation strategies do not work well in this context, and cooperative strategies are needed.

At the receiver, packet synchronization and "time-hopping" synchronization must be performed to properly decode the received signal. Packet synchronization consists of finding the correct time instant corresponding to the start of an incoming packet at the receiver. In general, this can be achieved through an energy-collection approach. During the packet synchronization, the transmitter sends an *a priori* known sequence, i.e., a preamble. After correlating the received signal and the expected signal, the receiver identifies the starting point of the packet as the time instant where the correlation is maximized. The second step consists of finding the time-hopping sequence to hop chip-by-chip and correlate the received pulses. This can be achieved by seeding the random generator with the same seed used by the transmitter, and therefore generating the same pseudorandom time-hopping sequence. More details are given in Section V-C. Once both synchronization processes have been accomplished, the receiver can decode the received signal by "listening" in the time chips of interest and by correlating the received pulse according to the modulation scheme in use.

Adaptive Channel Coding: An adaptive channel code [27] can further reduce the effect of mutual interference from co-located devices by dynamically regulating the coding rate to adapt to channel conditions and interference level. Various channel coding solutions have been proposed [24], [27]–[30] with different performance levels and computational complexity. We rely on simple *pseudo-orthogonal spreading codes* because of their excellent multiple access performance, limited computational complexity, and inherent resilience to multipath. Each bit is spread by multiplying it by a pseudorandom code before transmission. At the receiver side, with prior knowledge of the code used at the transmitter, the signal can be despread, and the original information recovered. With different pseudo-orthogonal codes, multiple nodes can transmit simultaneously on the same portion of the spectrum, with reduced interference. We explored two alternative modulation schemes, which we refer to as PPM-BPSK-spread and PPM-PPM-spread.

In PPM-BPSK-spread, the binary spreading code at the kth node, $\{a_j^{(k)}\}$, is defined as a pseudorandom code of $N_{\rm s}$ chips with $a_j \in \{-1, 1\}$. Accordingly, the information bit is spread using BPSK modulated chips, and by combining with time-hopping, (3) can be rewritten as

$$s^{(k)}(t,i) = \sum_{j=0}^{N_{\rm s}-1} a_j^{(k)} p(t - c_j^{(k)} T_{\rm c} - jT_{\rm f} - d_i^{(k)}\delta) \tag{5}$$

where δ is the PPM displacement of a pulse representing a "1" bit, while chip information is carried in the pulse polarity.

In PPM-PPM-spread, the information bit is spread using PPM-modulated chips. In this case, the binary spreading code can be defined as a pseudorandom code of $N_{\rm s}$ chips with $a_j \in \{-1, 1\}$. With time-hopping, (3) can be rewritten as

$$s^{(k)}(t,i) = \sum_{j=0}^{N_{\rm s}-1} p\left(t - c_j^{(k)} T_{\rm c} - jT_{\rm f} - \frac{a_j^{(k)} d_i^{(k)} + 1}{2}\delta\right). \tag{6}$$

In Fig. 6, we show an example of a combined time-hopping and PPM-BPSK-spread coding strategy. Since the spreading operation associates N_{s} chips with one information bit, the information rate will be further reduced by a factor N_{s}, i.e.,

$$R(N_{\mathrm{h}}, N_{\mathrm{s}}) = \frac{1}{N_{\mathrm{s}} T_{\mathrm{f}}} = \frac{1}{N_{\mathrm{s}} N_{\mathrm{h}} T_{\mathrm{c}}} \tag{7}$$

while the energy required for transmitting one bit is increased by a factor N_{s}. Note that there is a tradeoff between robustness to multiuser interference (which increases with longer spreading codes) and energy consumption and information rate. In Section V, we discuss joint dynamic adaptation of frame and code length. In both cases, PPM-PPM-spread and PPM-BPSK-spread, the receiver can use the spreading code employed at the transmitter to obtain the correlator template. With BPSK-modulated chips, the absolute received *phase information* is needed for decoding. Therefore, a *coherent* receiver with accurate channel knowledge is needed. Instead, with a pure PPM-modulated signal, a simple *non-coherent* energy detector receiver is sufficient. The latter requires frame synchronization only, and its hardware complexity is significantly lower [31].

Signal-to-Interference-Plus-Noise Ratio: We can express the signal-to-interference-plus-noise ratio (SINR) for impulsive transmissions at the receiver of link i as [24]

$$\mathrm{SINR}_i(\mathbf{N}_{\mathrm{h}}, \mathbf{N}_{\mathrm{s}}) = N_{\mathrm{s},i} \frac{P_i g_{i,i}\, N_{\mathrm{h},i} T_{\mathrm{c}}}{\eta + \sigma^2 T_{\mathrm{c}} \sum\limits_{k \in \mathcal{I}_i} P_k g_{k,i}} \tag{8}$$

where P_i is the average power per pulse period emitted by the ith transmitter, $g_{i,j}$ is the path gain between the ith transmitter and the jth receiver, η represents background noise energy, and σ^2 is an adimensional parameter that depends on the shape of the transmitted pulse and the receiver correlator. The set $\mathcal{I}_i$ represents the set of links whose transmitter interferes with the receiver of link i. Recall that $T_{\mathrm{f}} = N_h T_{\mathrm{c}}$ is the frame duration. When different links use different frame lengths, (8) becomes

$$\mathrm{SINR}_i(\mathbf{N}_{\mathrm{h}}, \mathbf{N}_{\mathrm{s}}) = N_{\mathrm{s},i} \frac{P_i g_{i,i}\, N_{\mathrm{h},i} T_{\mathrm{c}}}{\eta + \sigma^2 T_{\mathrm{c}} \sum\limits_{k \in \mathcal{I}_i} \frac{N_{\mathrm{h},i}}{N_{\mathrm{h},k}} P_k g_{k,i}}. \tag{9}$$

The expression in (9) depends on the array of frame and code lengths of all the ongoing communications in the network, i.e., $\mathbf{N}_{\mathrm{h}}, \mathbf{N}_{\mathrm{s}}$, whose ith elements are $N_{\mathrm{h},i}$ and $N_{\mathrm{s},i}$, respectively. The term $\frac{N_{\mathrm{h},i}}{N_{\mathrm{h},k}}$ accounts for the level of interference generated by each interferer k to the receiver of link i, i.e., the number of pulses transmitted by the kth transmitter during the time frame of the ith user. Note that we will not consider power control strategies in our treatment since [25] showed that in the linear regime, when the objective is to maximize the aggregate data rate, the optimal solution always corresponds to points where individual devices transmit at the maximum power or do not transmit at all.

Note that increasing (or decreasing) the spreading code length of the node of interest, $N_{\mathrm{s},i}$, leads to an increase (decrease) in the SINR. When the node of interest increases (decreases) its frame length $N_{\mathrm{h},i}$ while the other nodes do not, we expect no variation in the SINR (there is in fact a slight increase (decrease) in the SINR, which can be neglected under high-SNR conditions, $\eta \ll \sum_{k \in \mathcal{I}_i} P_k g_{ki}$). Finally, when the frame length of the interfering nodes is increased (decreased), the SINR increases (decreases).

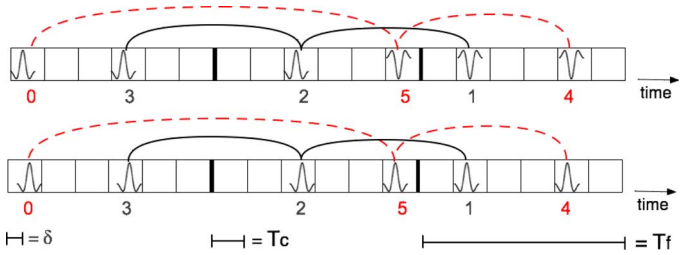

Fig. 6. Example of two ongoing transmissions *(top)* PPM-BPSK-spread and *(bottom)* PPM-PPM-spread with $d = 1$, $N_{\mathrm{h}} = 6$, $N_{\mathrm{s}} = 3$, using time-hopping sequences $TH_1 = \{3, 2, 1\}$ and $TH_2 = \{0, 5, 4\}$ and spreading codes $SC_1 = \{1, 1, -1\}$ and $SC_2 = \{1, -1, -1\}$.

Bit Error Rate: The bit error rate at the receiver can be approximated by evaluating the pulse collision probability when time hopping and channel coding are used. Consider first a pure time-hopping system with no pulse repetition, i.e., one transmitted pulse per bit. Assume that the information carried by a pulse cannot be decoded correctly only if two or more pulses from different users, representing different symbols, are transmitted in the same time chip. Under this hypothesis, considering K interferers using the same frame length N_{h}, the probability of collision is given by

$$P_{\mathrm{c}} = 1 - \sum_{i=0}^{|M|-1} p_i \left[1 - (1 - p_i)\frac{1}{N_{\mathrm{h}}}\right]^K \tag{10}$$

where p_i is the *a priori* probability of transmitting the ith symbol in the set of possible symbols M, e.g., $\{0, 1\}$, with $|M|$ the size of the set M, and $(1 - p_i)\frac{1}{N_{\mathrm{h}}}$ is the probability that one pulse collides (because the symbol is different), that is, the information carried by the pulse cannot be decoded correctly.

Since the collision probability depends on the number of pulses transmitted by an interferer within the user time frame, N_{h} in (10) represents the frame length of the node generating interference. Thus, if different nodes use different frame lengths, (10) can be rewritten as

$$P_{\mathrm{c}} = 1 - \sum_{i=0}^{|M|-1} p_i \prod_{j=0}^{G} [1 - (1 - p_i)1/N_{\mathrm{h},j}]^{K_j} \tag{11}$$

where $N_{\mathrm{h},j}$ is the frame length in number of chips used by the K_j nodes in the jth group and G is the number of groups into the network, where each group includes all the nodes in the network using the same frame length.

Finally, we consider the effect of pulse repetition. Assume that, for each bit, N_{s} pulses are sent, one per frame. The bit cannot be correctly decoded if more than half of the transmitted pulses collide. Since the probability of having x collisions over N_{s} transmissions follows a binomial distribution

$$P_x = \binom{N_{\mathrm{s}}}{x} P_{\mathrm{c}}^x (1 - P_{\mathrm{c}})^{N_{\mathrm{s}} - x} \tag{12}$$

the probability that more than half transmitted pulses collide is given by

$$P_{\frac{N}{2}+1} = \sum_{x = \left\lfloor \frac{N_{\mathrm{s}}}{2} + 1 \right\rfloor}^{N_{\mathrm{s}}} P_x. \tag{13}$$

Finally, the symbol error rate can be expressed as

$$P_{\text{err}} = 1 - \sum_{i=0}^{|M|-1} p_i \left[1 - (1-p_i) P_{\frac{N}{2}+1}\right]. \tag{14}$$

Note that this expression is exact for a simple repetition code. A pseudorandom spreading code increases the collision recovery capability at the receiver. Thus, the effective BER will be further reduced. The BER is a decreasing function of the code length of the transmission and of the frame length of the interfering nodes. Increasing the code length of the transmission and the frame length of the interfering nodes reduces the probability of collision. Increasing the frame length of the transmitter does not lead to any BER variation.

V. MAC and Rate Adaptation

In this section, we discuss UsWB medium access control principles and rate adaptation. Based on our discussion so far, there is a tradeoff between: 1) resilience to interference and channel errors; 2) achievable information rate; and 3) energy efficiency. We introduce medium access control and rate adaptation strategies designed to find optimal operating points along efficiency–reliability tradeoffs. We first consider rate-maximizing adaptation strategies in Section V-A. Then, we propose two different energy-minimizing strategies in Section V-B.

A. Distributed Rate-Maximizing Adaptation

The objective of the rate-adaptation algorithm under consideration is to let each active communication maximize its transmission rate by selecting a pair of code and frame lengths, based on the current level of interference and channel quality measured at the receiver and on the level of interference generated by the transmitter to the other ongoing communications. We consider a decentralized ultrasonic intrabody area network, with $\mathcal{N}$ being the set of $|\mathcal{N}|$ existing connections. Note that there are no predefined constraints on the number of simultaneous connections $|\mathcal{N}|$. The actual number $|\mathcal{N}|$ depends on the specific application. For example, in simple applications such as glucose measurements and insulin administration, the number $|\mathcal{N}|$ can be in the order of a few units. Instead, in more advanced applications, e.g., minimally intrusive microsurgery, the number of simultaneous existing connections can be higher. Denote by $N_{\text{h,max}}$ and $N_{\text{s,max}}$ the maximum frame and code lengths supported

$$0 < N_{\text{h},i} \leq N_{\text{h,max}} \qquad \forall i \in \mathcal{N},\ N_{\text{h}} \in \mathbb{N} \tag{15}$$

$$0 < N_{\text{s},i} \leq N_{s,\text{max}} \qquad \forall i \in \mathcal{N},\ N_{\text{s}} \in \mathbb{N} \tag{16}$$

where $\mathbb{N}$ is the set of natural numbers. According to the transmission scheme discussed in Section IV-A, each node i transmits at a rate R_i expressed as in (7), and each receiver experiences an SINR expressed as in (9). Each node has a minimum data rate requirement, i.e., $R_i(N_{\text{h},i}, N_{s,i}) \geq R_{\min}$, and a minimum SINR requirement, i.e., $\text{SINR}_i(\mathbf{N}_{\text{h},\mathbf{i}}, \mathbf{N}_{\mathbf{s},\mathbf{i}}) \geq \text{SINR}_{\min}$.

Explicitly Cooperative Problem: The receiver is in charge of estimating interference and calculating frame and spreading code lengths that maximize the system performance. Accordingly, we denote the frame length and the code length calculated by the receiver of the connection r, as $N_{\text{h},r}$ and $N_{\text{s},r}$.

The objective of each user is to locally optimize the information rate of the connection by solving the following problem:

$$\underset{N_{\text{h},r}, N_{\text{s},r}}{\text{maximize}} \quad R_r(N_{\text{h},r}, N_{\text{s},r}) \tag{17}$$

$$\text{subject to} \quad R_r(N_{\text{h},r}, N_{\text{s},r}) \geq R_{\min} \tag{18}$$

$$\text{SINR}_r(N_{\text{h},r}, N_{\text{s},r}) \geq \text{SINR}_{\min} \tag{19}$$

$$\text{SINR}_i(N_{\text{h},r}, N_{\text{s},r}) \geq \text{SINR}_{\min} \qquad \forall i \in \mathcal{I}_r \tag{20}$$

where $\mathcal{I}_r$ is the set of the connections interfering with the rth connection. The constraints on the maximum frame and code length in (15) and (16) are also implicitly considered. We refer to this as the *explicitly cooperative problem*.

Implicitly Cooperative Problem: If all nodes measure the same level of interference, that is, all network nodes are close enough to be all in the same transmission range, and all nodes have the same minimum rate and minimum SINR requirements, the level of interference that can be tolerated by each receiver is the same. Therefore, information about the maximum interference tolerable by each receiver does not need to be exchanged. The problem in (17) becomes then

$$\underset{N_{\text{h},r}, N_{\text{s},r}}{\text{maximize}} \quad R_r(N_{\text{h},r}, N_{\text{s},r})$$

$$\text{subject to} \quad R_r(N_{\text{h},r}, N_{\text{s},r}) \geq, R_{\min} \tag{21}$$

$$\text{SINR}_r(N_{\text{h},r}, N_{\text{s},r}) \geq \text{SINR}_{\min}. \tag{22}$$

The system of SINR inequality constraints in (17) becomes here a single inequality constraint. The new problem can be interpreted as *finding the optimal pair of code and frame length that maximize the rate, given a minimum rate and a minimum SINR, under the assumption that all the other nodes will be acting in the same way*. As we will show in Section VI, since the problem to be solved is the same for each node, a globally optimal pair of code and frame lengths will be found. We refer to this as the *implicitly cooperative problem*.

We now provide a detailed study of the explicitly cooperative problem. The implicitly cooperative problem can be derived as a special case by neglecting the constraint in (20).

The explicitly cooperative problem, stated in (17) as an integer program, i.e., variables $N_{\text{h},r}$ and $N_{\text{s},r}$, are constrained to assume integer values. If the domain of the problem is small, it can be solved by enumeration, i.e., trying all the possible combinations of $N_{\text{h},r}$ and $N_{\text{s},r}$. When the domain of the problem increases in size, a relaxation method can be used to transform the integer problem into a real-value problem. The relaxation operation consists of replacing the constraints in (15) and (16) with

$$0 < N_{\text{h},r} \leq N_{\text{h,max}} \quad 0 < N_{\text{s},r} \leq N_{\text{s,max}} \quad N_{\text{s},r}, N_{\text{h},r} \in \mathbb{R} \tag{23}$$

where $\mathbb{R}$ is the set of real numbers. Note that the optimal solution to the relaxed problem is not necessarily integer. However, since the feasible set of the relaxed problem is larger than the feasible set of the original integer program, the optimal value of the former, p^*_{rlx} is a lower bound on the optimal value of the latter, p^*_{int}, i.e.,

$$L = p^*_{\text{rlx}} \leq p^*_{\text{int}}. \tag{24}$$

The relaxed solution can be used to find an integer solution by rounding its entries based on a threshold $\theta \in [0,1]$, i.e.,

$$\hat{x}^*_{\text{int}} = \begin{cases} \lceil x^*_{\text{rlx}} \rceil, & \text{if } \lceil x^*_{\text{rlx}} \rceil - x^*_{\text{rlx}} \geq \theta \\ \lfloor x^*_{\text{rlx}} \rfloor, & \text{otherwise} \end{cases} \tag{25}$$

where $\lceil \cdot \rceil$ and $\lfloor \cdot \rfloor$ are the ceiling and floor functions, respectively. If the rounded solution, $\hat{x}^*_{\text{int}}$, is feasible for the original problem, i.e., all the constraints are satisfied, then it can be considered a guess at a good, if not optimal, point for the original problem. Moreover, the objective function evaluated at $\hat{p}^*_{\text{int}}$ is an upper bound on p^*_{int}

$$U = \hat{p}^*_{\text{int}} \geq p^*_{\text{int}}. \tag{26}$$

Therefore, $\hat{x}^*_{\text{int}}$ cannot be more than (U-L)-suboptimal for the original problem.

After the problem has been relaxed, we can express the relaxed problem as a geometric program [32], that is, minimizing a posynomial function under posynomial inequality constraints, by means of a change of variable and a transformation of the objective and constraints functions. After the transformation, we can efficiently solve the problem using polynomial-time interior-point algorithms [33].

First, the problem must be restated in terms of minimizing the inverse of the data rate, that is, $R_r^{-1}(N_{\text{h},r}, N_{\text{s},r})$. Then, the new objective function and all the constraints can be expressed in monomial and posynomial form. The objective function, as well as the minimum rate function, is a monomial function, $N_{\text{h},r}^{-1}\, N_{\text{s},r}^{-1}$. The same holds for the constraint functions defined is (23), and for the SINR function defined in (9).

Let us first consider the SINR constraint in (19). Note that in the distributed optimization problem the only variables are the code and the frame length calculated by the receiver, $N_{\text{s},r}$ and $N_{\text{h},r}$. If we define

$$\alpha_r = P_r g_{r,r} T_{\text{c}} \tag{27}$$

and

$$\beta_k = \frac{\sigma^2 T_{\text{c}} P_k g_{k,r}}{N_{\text{h},k}} \tag{28}$$

then (19) can be rewritten as a posynomial constraint

$$\eta N_{\text{s},r}^{-1} N_{\text{h},r}^{-1} + N_{\text{s},r}^{-1} \sum_{k \in \mathcal{I}_r} \beta_k \leq \frac{\alpha_r}{\text{SINR}_{\min}}. \tag{29}$$

For the remaining $(|\mathcal{I}_r| - 1)$ SINR constraints, if we define

$$\begin{aligned} \gamma_i &= P_i g_{i,i} T_{\text{c}} N_{\text{h},i} N_{\text{s},i} \quad \epsilon_i = \sigma^2 T_{\text{c}} P_r g_{r,i} N_{\text{h},i} \\ \delta_i &= \sum_{k \in \mathcal{I}_i} \sigma^2 T_{\text{c}} P_k g_{k,i} N_{\text{h},i} / N_{\text{h},k} \end{aligned} \tag{30}$$

then (20) can be rewritten as

$$\frac{\eta + \delta_i + \epsilon_i N_{\text{h},r}^{-1}}{\gamma_i} \leq \frac{1}{\text{SINR}_{\min}} \tag{31}$$

which is a linear, and thus monomial, constraint. In particular, this constraint shows that the frame length variation only leads to an increase (decrease) in the level of interference produced. Moreover, constraint (31) suggests that the optimal frame length is constrained by the co-located node that is experiencing the highest level of interference. Based on these observations, the cooperative optimization problem becomes

$$\underset{N_{\text{h},r}, N_{\text{s},r}}{\text{minimize}} \quad R_r^{-1}(N_{\text{h},r}, N_{\text{s},r}) \tag{32}$$

$$\text{subject to} \quad R_r^{-1}(N_{\text{h},r}, N_{\text{s},r}) \leq R_{\min}^{-1} \tag{33}$$

$$\eta N_{\text{s},r}^{-1} N_{\text{h},r}^{-1} + N_{\text{s},r}^{-1} \sum_{k \in \mathcal{I}_r} \beta_k \leq \frac{\alpha_r}{\text{SINR}_{\min}} \tag{34}$$

$$N_{\text{h},r} \geq \frac{\epsilon_i}{\gamma_i \, \text{SINR}_{\min}^{-1} - \eta - \delta_i}. \tag{35}$$

Finally, a geometric program can be in general transformed into a convex program through a logarithmic transformation of the optimization variables. If we define

$$\mathbf{y} = [y_1 \; y_2] = [\log N_{\text{h},r} \; \log N_{\text{s},r}] \tag{36}$$

the objective function and the rate constraint function become

$$R_r^{-1}(N_{\text{h},r},\, N_{\text{s},r}) = N_{\text{h},r} \quad N_{\text{s},r} = e^{y_1} e^{y_2} = e^{\mathbf{a_0^T y}} \tag{37}$$

where $a_0 = [1 \; 1]$. The constraint function in (34) becomes

$$\begin{aligned} \eta N_{\text{s},r}^{-1} N_{\text{h},r}^{-1} + N_{\text{s},r}^{-1} \sum_{k \in \mathcal{I}_r} \beta_k &= \eta (e^{y_1})^{-1} (e^{y_2})^{-1} + \sum_{k \in \mathcal{I}_r} \beta_k (e^{y_2})^{-1} \\ &= e^{\mathbf{a_1^T y} + b_1} + e^{\mathbf{a_2^T y} + b_2} \end{aligned} \tag{38}$$

where $a_1 = [-1 \; -1]$, $a_2 = [0 \; -1]$, $b_1 = \log \eta$ and $b_2 = \log \sum_{k \in \mathcal{I}_r} \beta_k$. Then, one can transform the problem by taking the logarithm of the objective function and the constraint functions. The resulting problem can be expressed as

$$\underset{\mathbf{y}}{\text{minimize}} \quad \mathbf{a_0^T} \; \mathbf{y} \tag{39}$$

$$\tag{40}$$

$$\text{subject to} \quad \mathbf{a_0^T} \; \mathbf{y} \leq R_{\min}^{-1} \tag{41}$$

$$\log \left(e^{\mathbf{a_1^T y} + b_1} + e^{\mathbf{a_2^T y} + b_2} \right) \leq \log \frac{\alpha_r}{\text{SINR}_{\min}} \tag{42}$$

$$y_1 \geq \log \left(\frac{\epsilon_i}{\gamma_i \, \text{SINR}_{\min}^{-1} - \eta - \delta_i} \right) \tag{43}$$

$$0 \leq y_1 \leq \log N_{\text{h,max}}, \qquad y_1 \in \mathbb{R} \tag{44}$$

$$0 \leq y_2 \leq \log N_{\text{s,max}}, \qquad y_2 \in \mathbb{R} \tag{45}$$

$$\forall i \in \mathcal{I}_r. \tag{46}$$

The objective function and the constraint function in (40) are linear, thus also convex. The constraint in (42) is convex as a result of the transformation performed [32]. We can conclude that the this problem is a convex optimization problem that can be solved in polynomial time through interior-point methods [33].

B. Distributed Energy-Minimizing Rate Adaptation

We now concentrate on rate adaptation with the objective of reducing the energy consumption of UsWB. We mentioned in Section IV-A that the time-hopping and the spreading code techniques affect the energy consumption of the device transmitting a UsWB signal. For this reason, we introduce energy-related metrics that make the dependence of the energy consumption on code and frame length explicit. We define the following:

- E_{p}, the energy per pulse;
- E_{b}, the energy per bit, i.e., $E_{\text{b}} = E_{\text{p}} \cdot N_{\text{s}}$;

- E_{s}, the average power radiated per second, i.e., $E_{\mathrm{s}} = E_{\mathrm{p}}/(T_{\mathrm{c}} \cdot N_{\mathrm{h}})$.

The energy per bit is a linear function of the spreading code length, therefore of the number of pulses transmitted per each bit. The average power emitted per second is a function of the inverse of the frame length and hence of the number of pulses transmitted per second. Both depend on the value of E_{p}, which is related to the (electrical) power absorption of the ultrasonic transducer in use.

Modeling the Energy Consumption of a Piezoelectric Transducer: We consider electronically driven piezoelectric transducers. Since such devices are known to have minimal current leakage, the majority of power consumption comes from the piezoelectric element. Outside the region of resonance, a piezoelectric ceramic transducer can be viewed (from the electrical point of view) as a parallel plate capacitor with capacitance C_0. Thus, the main source of power consumption comes from charging such a capacitor [34]. Then, ignoring charge and discharge losses, and considering a capacitor with voltage supply V and pulse repetition frequency f (which corresponds to the charge and discharge frequency of the capacitor), the power consumption P_{c} can be expressed as

$$P_{\mathrm{c}} = f C_0 V^2. \tag{47}$$

The static capacitance and the voltage supply values should be based on transducer-specific considerations. The static capacitance value of a disc-shaped transducer is

$$C_0 = \frac{A \epsilon_0 K}{t_h} \quad [F] \tag{48}$$

where ϵ_0 is the permittivity in free air (8.8542 F/m), K is the dielectric constant of the material (adimensional), A [m^2] is the area of the disc, and t_h [m] is its thickness. The dielectric constant K depends on material, frequency, and mechanical state of the transducer.

We derive appropriate limits for the voltage supply based on safety concerns, which impose a limit on the radiated acoustic power. As reported in [4], no tissue damage occurs in intrabody ultrasonic propagation as long as the acoustic power dissipation in tissues is limited to 10^4 W/m^2. From this limit, we derive the corresponding maximum pressure magnitude that can be radiated by the transducer, and consequently the maximum voltage input. For example, if we consider arm muscle as the primary propagation medium, by using the quadratic relation between the acoustic intensity and the acoustic pressure, $I = (P_{\mathrm{RMS}})^2/\rho c$, along with density and speed of sound parameters in [21], we find a maximum pressure magnitude of approximately 0.13 MPa.

We can derive the related transducer voltage input, corresponding to the maximum radiated pressure, through the constitutive equation of piezoelectric materials. The latter expresses the relationship between mechanical strain and electrical displacement for the piezoelectric element considering the electrical and mechanical stress and is usually expressed in tensor notation [35]. Here, we are interested in the so-called *converse effect*, i.e., the material strain proportional to an applied voltage. If we consider a symmetric crystal structure, the constitutive relations reduce to a few parameters. In particular, the so-called g_{33} parameter [Vm/N] represents the piezoelectric voltage coefficient, when the polarization field and the piezoelectrically induced strain are both parallel to the disc axis (usually referred to as the third axis). Based on this, one can express the electric field along the third axis E [V/m] as $E = g_{33} P$, where P again represents the output pressure of the transducer. Since the electric field E can in turn be expressed as the ratio between voltage and electrode distance, we have $V = g_{33}\, P t_h$. Finally, from (47), the energy necessary to generate a single pulse is obtained as

$$E_{\mathrm{p}} = C_0 (g_{33} P t_h)^2 \quad [\mathrm{J}]. \tag{49}$$

Energy-Minimizing Rate Adaptation: Based on this model, we design a rate adaptation strategy where the objective is to minimize: 1) the energy per bit E_{b}, or 2) the average energy emitted per second E_{s}. The problem can be cast as finding the optimal frame length and the optimal spreading code length that minimize E_{b} (and/or E_{s}) while meeting the minimum SINR constraints and keeping the data rate over a given threshold. The problem is formally expressed as follows:

$$\begin{aligned} \underset{N_{\mathrm{h},r}, N_{\mathrm{s},r}}{\text{minimize}} \quad & E_{\mathrm{b}}(N_{\mathrm{s},r}) \text{ (or } E_{\mathrm{s}}(N_{\mathrm{h},r})) \\ \text{subject to} \quad & (18)\text{–}(20). \end{aligned}$$

The problem above can also be relaxed to a geometric program as discussed in Section V-A.

C. Medium Access Control Protocol

In UsWB, distributed medium access control coordination is achieved by exchanging information on logical *control channels*, while data packets are transmitted over logical *data channels*. We consider unicast transmissions between a transmitter TX and a receiver RX. When TX needs to transmit a packet, it first needs to reserve a dedicated channel to RX. The connection is opened through the common control channel, which is implemented through a unique TH-sequence and a spreading code known and shared by all network devices.

In the two-way handshake procedure, TX sends a Request-to-Transmit (R2T) packet to RX, which contains its own ID. If RX is idle, a Clear-to-Transmit (C2T) control packet is sent back to TX. In case of failure and consequent timer expiration, TX will attempt a new transmission after a random backoff time, for a maximum of N_R times. During these initial steps, since an estimate of the current interference level is not available, the transmitter transmits at the minimum data rate, conservatively using a maximum frame length and spreading code length, and thus generating low interference. After receiving the C2T packet, the transmitter switches to a dedicated channel by computing its own time-hopping sequence and spreading code obtained by seeding a pseudorandom sequence generator with its own ID. As a consequence, both TX and RX leave the common channel and switch to a dedicated channel. Once the connection has been established, TX sends the first packet using maximum frame and spreading code length. The receiver RX computes the optimal frame and spreading code lengths as discussed in Section IV-A. This information is piggybacked into ACK or NACK packets.

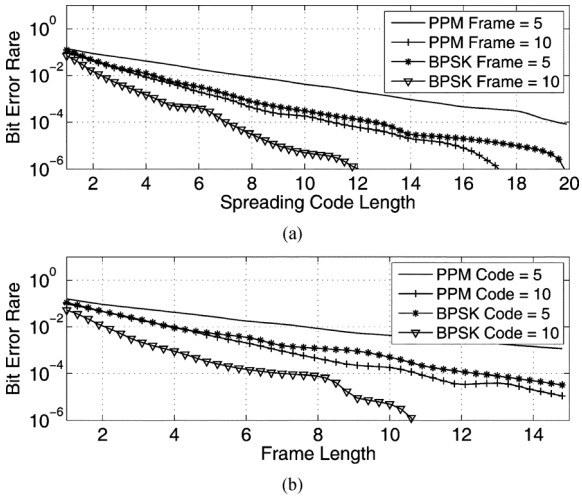

Fig. 7. *(top)* BER versus spreading code length and *(bottom)* BER versus time-hopping frame length for PPM-BPSK spread and PPM-PPM spread.

In the explicitly cooperative case, discussed in Section V-A, once the communication has been established, RX does not leave the common control channel. Instead, it keeps "listening" to both the dedicated and common control channels at the same time. In the dedicated control channel, RX sends to TX the optimal frame and code lengths to be used for the next transmission. In the common control channel, RX exchanges with other co-located receivers information on the level of tolerable interference.

VI. Performance Evaluation

A. Multiscale Simulator

In this section, we evaluate the proposed system performance through a custom-designed multiscale simulator that models UsWB performance at three different levels, i.e.: 1) at the *acoustic wave level* by capturing ultrasonic propagation in tissues through reflectors and scatterers; 2) at the *bit level* by simulating in detail the physical layer transmission scheme; 3) at the *packet level* by simulating networked operations and distributed medium access control and adaptation.

The acoustic wave level simulation is performed as described in Section III. A channel impulse response is obtained by simulating propagation in the human arm. Transmission at the bit level is modeled through a custom physical-layer simulator of UsWB, which produces as output an empirical model of the BER against different values of the time-hopping frame length and spreading code length, for different levels of interference. The physical-layer simulation models a transmitter and a receiver (located 20 cm apart) communicating over an ultrasonic channel with the UsWB transmission scheme. Simulations are performed to obtain an estimate of the achievable BER upon varying the frame length and the spreading code length with a different number of interferers transmitting on the same channel. The interfering nodes are located within the interference range area of the receiving node of the pair, i.e., they are also located 20 cm apart from the receiving node. In the simulations, we neglect both frame and time-hopping synchronization errors so that the BER only considers interference effects. We implement both solutions presented in Section IV-A, i.e., PPM-BPSK-spread with coherent receiver and the PPM-PPM-spread with noncoherent receiver. An extensive simulation campaign was conducted, and BER values were obtained as a function of the spreading code and frame lengths for different numbers of simultaneously active connections. Fig. 7 reports the BER values measured at the receiver, when three interfering nodes transmit at the same time and are located in the interference range area of the receiving node. As expected, the coherent PPM-BPSK-spread slightly outperforms the noncoherent PPM-PPM-spread.

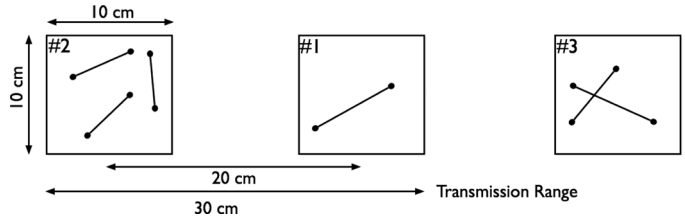

Fig. 8. Network simulation topology.

Network Simulation Topology: The empirical model of the BER as a function of frame length and spreading code length for a given level of interference is then imported in a Java-based event-driven packet-level simulator, which models all the UsWB MAC protocol functionalities. We considered two different settings for the network level simulations. First, we consider a 2-D topology with 18 static nodes randomly located inside a square of side 20 cm. Each transmitter node communicates with a randomly selected receiver node, in a point-to-point and single-hop fashion, resulting in a maximum of nine simultaneously communicating pairs. We also assume that the transmission range is greater than the maximum distance between the nodes. Thus, all nodes measure the same number of interferers.

The second setting consists of three 2-D squared clusters of nodes with side 10 cm, displaced 20 cm apart from each other (distance center-to-center). In each cluster, the nodes are randomly deployed according to a Gaussian distribution. The cluster (#1) in the middle contains one communicating pair, while clusters (#2) and (#3) contain a variable number of communicating pairs. We also assume the transmission range to be of 30 cm. Thus, all the nodes of adjacent clusters interfere with each other, while nodes of nonadjacent clusters do not. Under this assumption, communicating pairs from different clusters measure different levels of interference. As a result, this second scenario topology, depicted in Fig. 8, operates under the conditions of the explicitly cooperative problem. In a practical application, a similar scenario could for example represent three groups of ultrasonic sensors deployed in the heart, liver, and kidney, respectively.

During the simulations, frame length and spreading code length are adapted to the interference level measured at the receiver according to one of the objectives discussed in Section V-A. The simulation time is set to 100 s, and nodes start establishing connections at a random time instant, but no later than 2 s after the simulation start time. We consider an infinite arrival rate at each transmitter, i.e., transmitters are always backlogged. The maximum allowed frame and spreading code

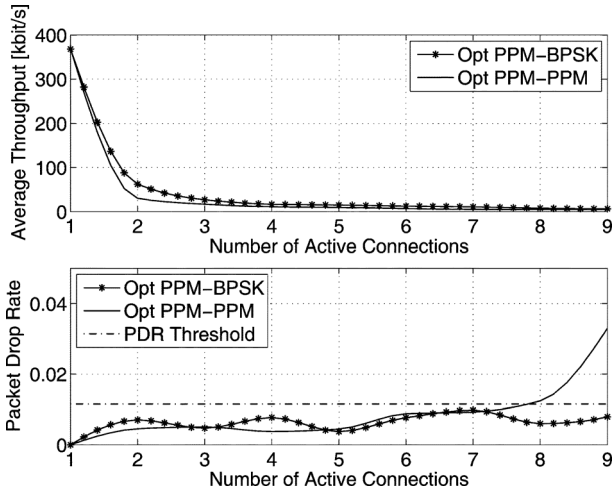

Fig. 9. *(top)* Average throughput [kb/s] and *(bottom)* packet drop rate with rate-maximizing solution for implicitly cooperative problem.

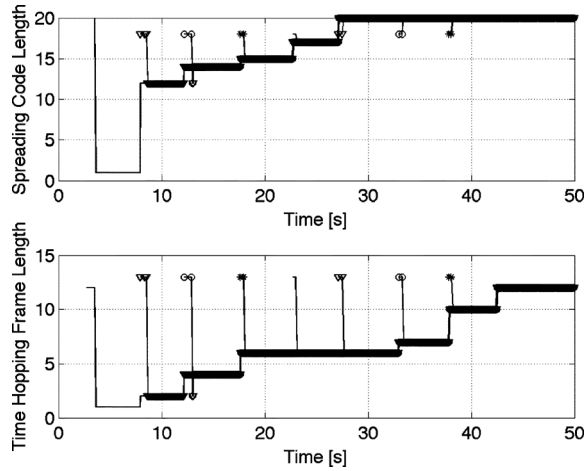

Fig. 10. Time evolution of *(top)* spreading code and *(bottom)* time-hopping frame lengths for the implicitly cooperative problem.

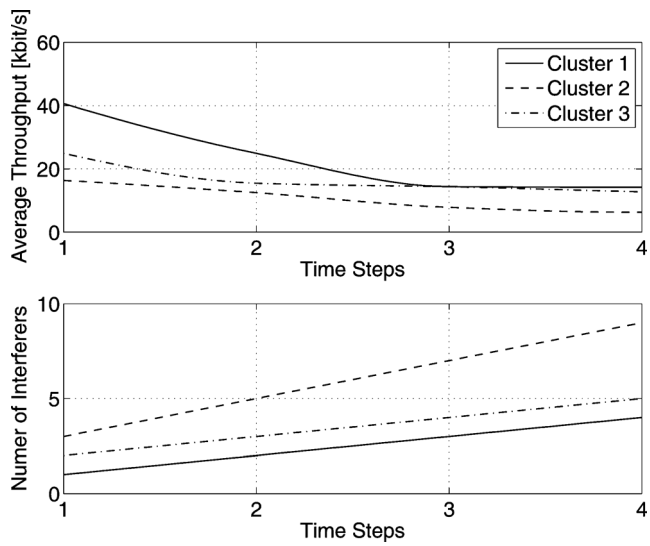

Fig. 11. *(top)* Average throughput [kb/s] and *(bottom)* number of interferers with explicitly cooperative problem for different time-steps.

length is set to 15 slots and 20 chips, respectively. The maximum supported rate, achieved when frame and spreading code length are both set to one, is equal to 2 Mb/s. The minimum SINR constraint leads to a maximum BER constraint of 10^{-5}.

We first discuss the performance in terms of throughput and packet drop rate of the rate-maximizing solution coming from both the implicit and explicit cooperative problems. We define the throughput as the average rate of information correctly received during the simulation time per active connection. The packet drop rate is defined as the ratio between the number of packets dropped and the number of packets generated at the application layer, averaged over all the active connections. Both performance metrics are evaluated as a function of the number of active connections $|\mathcal{N}|$.

1) Rate Maximization:

Implicitly Cooperative Solution: In Fig. 9, we compare network throughput (top) and packet drop rate (bottom) for the rate-maximizing strategy, when frame and code length are adaptively regulated based on the implicitly cooperative problem in Section V-A. Fig. 9 (bottom) also shows the maximum packet drop rate threshold given by the 10^{-5} BER constraint at the PHY layer. The rate-maximizing solution is presented for both the transmission schemes discussed in Section IV-A, i.e., the PPM-BPSK-spread with coherent receiver and the PPM-PPM-spread with noncoherent receiver. As expected, the coherent PPM-BPSK solution performs better in terms of throughput. This happens because the BER constraint is satisfied for lower values of frame length and code length, which leads to higher data rates according to (7). When the number of active connections is equal to one, i.e., there are no interferers, both systems achieve the same throughput since the same optimal pair is used, (2, 2). In terms of packet drop rate, for the coherent PPM-BPSK system, the BER constraint is satisfied for any number of active connections considered. Instead, for the noncoherent PPM-PPM system, when the number of active connections is greater than 7, the BER constraint cannot be satisfied anymore, and therefore the packet drop rate increases. Note that this problem can be overcome by simply relaxing the constraint on the maximum size of code length or frame length, without relaxing the constraint on the maximum BER. Clearly, this leads to a lower data rate.

We then focus on the analysis of the dynamic adaptation of the frame and code length performed distributively by each node. Focusing on the coherent system, in Fig. 10, we show the evolution in time of frame and code length when nine different connections are asynchronously activated with a deterministic 5-s delay between each other. As expected, each connection starts with the maximum supported frame and code length and then adaptively reaches the optimal value based on the interference level measured at the receiver. Since the number of interferers is the same for each receiver, the locally optimal solution is also globally optimal.

Explicitly Cooperative Solution: In Fig. 11, we plot the network throughput obtained when frame and code length are adaptively regulated based on the explicitly cooperative problem in (17). The solution is presented for the PPM-BPSK-spread transmission strategy discussed in Section IV-A. Throughput is evaluated by varying the number of active connections in four

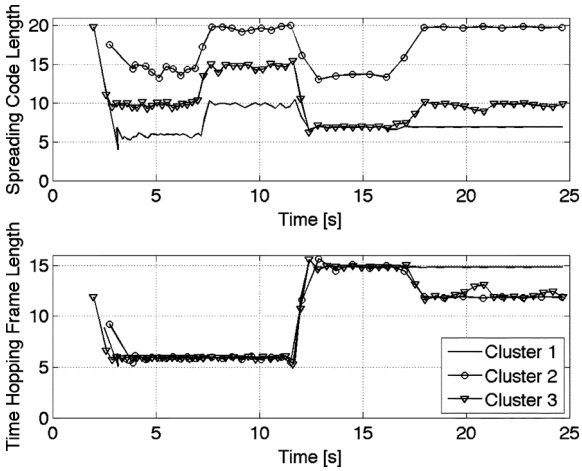

Fig. 12. Time evolution of *(top)* spreading code and *(bottom)* time-hopping frame lengths for the explicitly cooperative problem.

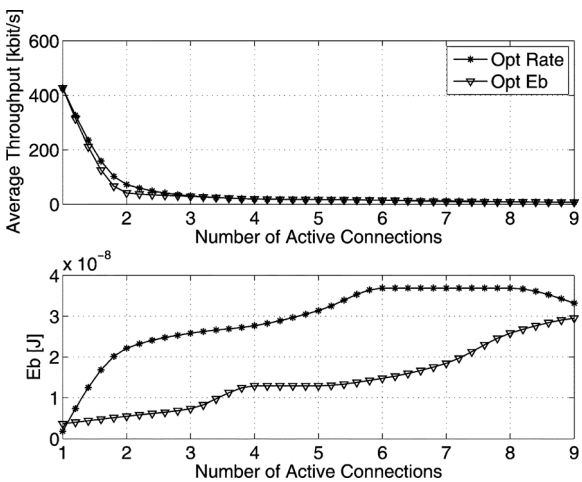

Fig. 13. Throughput and E_{b} vs. the number of active connections for rate maximizing and energy minimizing strategies.

consecutive time-steps. In particular, we assume that there is always one active connection in cluster #2. Clusters #1 and #3 activate a new connection at each time-step. In Fig. 11, we also report the average number of interferers measured by the receivers in each cluster. As expected, the cluster located in the middle, hence located within the transmission range of both the other two clusters, measures a higher level of interference, and therefore achieves a lower throughput. However, since the BER constraint is satisfied by all nodes in the three clusters, a low packet drop rate is achieved. Finally, in Fig. 12, the dynamic behavior of the frame and code length adaptation is shown. We consider two new connections activated asynchronously every 5 s in Clusters #1 and #3. In each cluster, the frame and code length are adapted according to the increasing level of interference measured in the channel. In particular, we observe the effect of the constraint in (35), which forces the frame length to be greater than or equal to the frame length of the connection that is experiencing the highest level of interference, i.e., the connection in Cluster #2.

2) Rate-Optimal Versus Energy-Optimal Results: In Fig. 13, we plot the throughput obtained by adapting the transmission

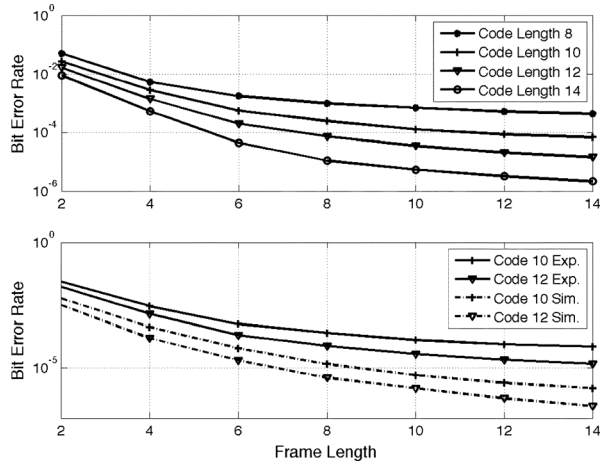

Fig. 14. *(top)* BER as a function of frame length, with four interfering pulses per frame for different values of code length, *(bottom)* compared to simulated BER.

rate according to the energy-minimizing strategy introduced in Section V-B. The energy-minimizing strategy is also compared to the rate-maximizing strategy introduced in Section V-A in terms of data rate and energy consumption. Both results are presented for the PPM-BPSK-spread transmission strategy. The throughput achievable in case of the rate-maximizing solution is comparable to what is obtained with the energy-optimized solution. When the number of active connections N is lower than 2, the throughput of the E_{b}-optimal strategy is close to the throughput of the rate-maximizing scheme. For N higher than 2, the two considered strategies show a similar throughput performance. Since the maximum BER constraint is always satisfied, the rate-maximizing and the energy-minimizing strategies lead to packet drop rates close to zero. Finally, the energy consumption obtained with the E_{b}-optimal solution is always better that what can be obtained using the rate-maximizing scheme. This result assumes that each node transmits at the maximum power allowed that gives a value of energy per pulse of $E_{\mathrm{p}} = 1.8436$ nJ obtained using the model presented in Section V-B assuming $A = 0.201$ mm^2, $A = 0.47$ mm, $K = 1800$, and $g_{33} = 0.027$ N/m.

B. Ultrasonic Software-Defined Testbed

Since no off-the-shelf ultrasonic transceivers for intrabody communications are available, we designed and developed our custom ultrasonic software-defined nodes based on the USRP N210 platform [36], as discussed in detail in [37]. In the following, we report BER experimental measurements obtained by varying the time-hopping frame and spreading code length in presence of interference. We compare these experimental results to BER curves obtained by simulating the same setup with the multiscale simulator discussed in Section VI-A, thus validating our simulation results. The experimental setup consists of two ultrasonic nodes that communicate through a human-kidney phantom [23]. The two ultrasonic transducers are located on opposite sides of the phantom at a distance of 10 cm. To guarantee repeatability of the experiments, we generate interference from co-located transceivers by artificially injecting interfering

pulses at the transmitter. The interfering pulses are pseudorandomly located inside the time-hopping frame. We evaluate the BER by varying the time-hopping frame, from 2 to 14, and the spreading code length between 8, 10, 12, and 14. We consider four interfering pulses per frame, and we set the input power at the TX transducer to 13 dBm ($\approx$ 20 mW). Results are shown in Fig. 14(a). In Fig. 14(b), the experimental results are compared to BER curves obtained by simulating the same scenario with the UsWB PHY-layer simulator described in Section VI-A. For fairness, the pulse shape used in the simulator is obtained by recording a real pulse shape as received in testbed experiments, thus considering the signal distortion introduced by amplifiers and transducers, and the scattering and reflection effects introduced by the ultrasonic phantom. However, the simulation setup does not consider the time-variability of the real testbed conditions, e.g., operating temperature, coupling of the transducer with the phantom surface, and partial synchronization failures. We observe that, as expected, the BER is a decreasing function of the time-hopping frame length and the spreading code length, thus confirming the simulation results in Section VI-A.

VII. Related Work

Previous work has suggested to use ultrawideband (UWB) communications in medical applications [38] because of their resilience to multipath and interference. In particular, UWB has been proposed for capsule endoscopy [39] to transmit real-time video imaging of the gastrointestinal tract or to detect tiny movements inside the body, e.g., to monitor cardiovascular physiological parameters, or for breast cancer diagnosis. However, strong attenuation negatively affects the performance of UWB inside the human body, leading to low data rates. Moreover, clear channel assessment techniques cannot be used since it is difficult to detect UWB pulses because of the very low power spectral density. Also, high synchronization delays make CSMA/CA schemes ineffective in case of short packets [40].

Regarding our integrated MAC- and PHY-layer scheme, there are several characteristics that separate it from the existing literature. First, UsWB is the first MAC/PHY-layer scheme for intrabody communications based on ultrasonic waves, instead of the commonly used RF electromagnetic waves. Second, the proposed PHY-aware MAC-layer solution is based on dynamically and distributively adapting physical-layer parameters, i.e., the time-hopping frame length and spreading code length, to enable multiple users to coexist without the need for mutual temporal exclusion between different transmissions. Last, another unique feature of UsWB is the joint optimization of time-hopping frame and spreading code length to control the tradeoffs among: 1) resilience to multiuser interference and ultrasonic channel errors; 2) achievable information rate; and 3) energy efficiency.

VIII. Conclusion

We proposed a paradigm shift in networking through body tissues to address the limitations of RF propagation in the human body. We presented—to the best of our knowledge—the first attempt at enabling networked intrabody communications among miniaturized sensors and actuators using ultrasonic waves.

We assessed the feasibility of using ultrasonic communications within the human body; we derived an accurate channel model for ultrasonic communications in the human body and built on it to propose a new ultrasonic transmission and multiple access technique, denoted as UsWB, based on transmission of short-duration pulses following a time-hopping pattern. Simulation and experimental results demonstrate the feasibility of ultrasonic communication in the human body and show how, by designing appropriate *ad hoc* transmission schemes and protocols, ultrasounds can be efficiently used to wirelessly internetwork implantable devices.

References

[1] G. E. Santagati, T. Melodia, L. Galluccio, and S. Palazzo, "Distributed MAC and rate adaptation for ultrasonically networked implantable sensors," in *Proc. IEEE SECON*, New Orleans, LA, USA, Jun. 2013, pp. 104–112.

[2] S. K. Gupta, T. Mukherjee, and K. K. Venkatasubramanian, *Body Area Networks: Safety, Security, and Sustainability*. Cambridge, U.K.: Cambridge Univ. Press, 2013.

[3] L. Galluccio, T. Melodia, S. Palazzo, and G. E. Santagati, "Challenges and implications of using ultrasonic communications in intra-body area networks," in *Proc. IEEE/IFIP WONS*, Courmayeur, Italy, Jan. 2012, pp. 182–189.

[4] T. Hogg and R. A. Freitas, "Acoustic communication for medical nanorobots," *Nano Commun. Netw.*, vol. 3, no. 2, pp. 83–102, Jun. 2012.

[5] IEEE, Piscataway, NJ, USA, "IEEE standard for safety levels with respect to human exposure to radio frequency electromagnetic fields, 3 kHz to 300 GHz," Tech. Rep., 1999.

[6] T. Melodia, H. Kulhandjian, L. Kuo, and E. Demirors, "Mobile ad hoc networking: cutting edge directions," in *Advances in Underwater Acoustic Networking*, S. Basagni, M. Conti, S. Giordano, and I. Stojmenovic, Eds. Hoboken, NJ, USA: Wiley, 2013.

[7] G. Oberholzer, P. Sommer, and R. Wattenhofer, "SpiderBat: Augmenting wireless sensor networks with distance and angle information," in *Proc. IPSN*, Apr. 2011, pp. 211–222.

[8] J. M. Reid, "Medical ultrasonics: Diagnostic applications of ultrasound," *Proc. IRE*, vol. 47, no. 11, pp. 1963–1967, Nov. 1959.

[9] F. L. Thurstone and H. E. Melton, "Biomedical ultrasonics," *IEEE Trans. Ind. Electron. Control Instrum.*, vol. IECI-17, no. 2, pp. 167–172, Apr. 1970.

[10] E. Lacaze, S. Michau, and P. Mauchamp, "20 MHz ultrasound array for medical imaging from design to image evaluation," in *Proc. IEEE Ultrasonics Symp.*, Atlanta, GA, USA, Oct. 2001, pp. 1139–1142.

[11] G. Lockwood, D. Turnball, D. Christopher, and F. Foster, "Beyond 30 MHz [applications of high-frequency ultrasound imaging]," *IEEE Eng. Med. Biol. Mag.*, vol. 15, no. 6, pp. 60–71, Nov.–Dec. 1996.

[12] R. Smith, A. Arca, X. Chen, L. Marques, M. Clark, J. Aylott, and M. Somekh, "Design and fabrication of nanoscale ultrasonic transducers," *J. Phys., Conf. Ser.*, vol. 353, p. 012001, 2012.

[13] K. K. Shung, *Diagnostic Ultrasound: Imaging and Blood Flow Measurements*. Boca Raton, FL, USA: CRC Press, 2006.

[14] A. Y. Cheung and A. Neyzari, "Deep local hyperthermia for cancer therapy: External electromagnetic and ultrasound techniques," *Cancer Res.*, vol. 44, no. 9, pp. 4736s–4744s, Oct. 1984.

[15] D. T. Blackstock, *Fundamentals of Physical Acoustics*. New York, NY, USA: Wiley-Interscience, 2000.

[16] C. R. Hill, *Ultrasonic Attenuation and Scattering by Tissues*. New York, NY, USA: Wiley, 1978.

[17] Olympus, Waltham, MA, USA, "Ultrasonic transducers technical notes," Tech. Rep., 2006 [Online]. Available: http://www.olympus-ims.com/data/File/panametrics/UT-technotes.en.pdf

[18] Y. Davilis, A. Kalis, and A. Ifantis, "On the use of ultrasonic waves as a communications medium in biosensor networks," *IEEE Trans. Inf. Technol. Biomed.*, vol. 14, no. 3, pp. 650–656, May 2010.

[19] B. T. Cox, S. Kara, S. R. Arridge, and P. C. Beard, "k-space propagation models for acoustically heterogeneous media: Application to biomedical photoacoustics," *J. Acoust. Soc. Amer.*, vol. 121, no. 6, p. 3453, Feb. 2007.

[20] B. Treeby and B. Cox, "k-Wave," [Online]. Available: http://www.k-wave.org/

[21] National Physical Laboratory, Teddington, U.K., "Tables of physical & chemical constants. 2.1.2 Barometry, Cpt. 2. Sec 4.6," [Online]. Available: http://www.kayelaby.npl.co.uk
[22] T. F. Rappaport, *Wireless Communications: Principles and Practice*. Upper Saddle River, NJ, USA: Prentice-Hall, 1999.
[23] CIRS, Norfolk, VA, USA, "Kidney training phantom," Tissue Simulation & Phantom Technology.
[24] M. Z. Win and R. A. Scholtz, "Ultra-wide bandwidth time-hopping spread-spectrum impulse radio for wireless multiple-access communications," *IEEE Trans. Commun.*, vol. 48, no. 4, pp. 679–689, Apr. 2000.
[25] F. Cuomo, C. Martello, A. Baiocchi, and F. Capriotti, "Radio resource sharing for ad hoc networking with UWB," *IEEE J. Sel. Areas Commun.*, vol. 20, no. 9, pp. 1722–1732, Dec. 2002.
[26] J. A. Gallo, D. O. Draper, L. T. Brody, and G. W. Fellingham, "A comparison of human muscle temperature increases during 3-MHz continuous and pulsed ultrasound with equivalent temporal average intensities," *J. Orthopaedic Sports Phys. Therapy*, vol. 395, no. 7, pp. 395–401, Jul. 2004.
[27] R. Merz, J. Widmer, J.-Y. Le Boudec, and B. Radunovic, "A joint PHY/MAC architecture for low-radiated power TH-UWB wireless ad hoc networks," *Wireless Commun. Mobile Comput.*, vol. 5, no. 5, pp. 567–580, 2005.
[28] N. Yamamoto and T. Ohtsuki, "Adaptive intemally turbo-coded ultra wideband-impulse radio (AITC-UWB-IR) system," in *Proc. IEEE ICC*, Anchorage, AK, USA, May 2002, pp. 3535–3539.
[29] E. Baccarelli and M. Biagi, "A simple adaptive coding scheme for multiuser interference suppression in ultra-wideband radio transmissions," *IEEE Trans. Commun.*, vol. 53, no. 8, pp. 1283–1287, Aug. 2005.
[30] X. Shen, W. Zhuang, H. Jiang, and J. Cai, "Medium access control in ultra-wideband wireless networks," *IEEE Trans. Veh. Technol.*, vol. 54, no. 5, pp. 1663–1677, Sep. 2005.
[31] L. Yang and G. Giannakis, "Ultra-wideband communications: an idea whose time has come," *IEEE Signal Process. Mag.*, vol. 21, no. 6, pp. 26–54, Nov. 2004.
[32] S. Boyd, S.-J. Kim, L. Vandenberghe, and A. Hassibi, "A tutorial on geometric programming," *Optimiz. Eng.*, vol. 8, pp. 67–127, 2007.
[33] Y. Nesterov and A. Nemirovskii, *Interior-Point Polynomial Algorithms in Convex Programming*. Philadelphia, PA, USA: SIAM, 1994, vol. 13, SIAM Studies in Applied Mathematics.
[34] J. Johansson and J. Delsing, "Microelectronics mounted on a piezoelectric transducer: Method, simulations, and measurements," *Ultrasonics*, vol. 44, no. 1, pp. 1–11, Jan. 2006.
[35] T. Jordan and Z. Ounaies, *Characterization of Piezoelectric Ceramic Materials*. New York, NY, USA: Wiley, 2002.
[36] Ettus, Santa Clara, CA, USA, "USRP: Universal software radio peripheral," [Online]. Available: http://www.ettus.com/
[37] G. E. Santagati and T. Melodia, "Sonar inside your body: Prototyping ultrasonic intra-body sensor networks," in *Proc. IEEE INFOCOM*, Toronto, ON, Canada, Apr. 2014, to be published.
[38] R. Chávez-Santiago, I. Balasingham, and J. Bergsland, "Ultrawideband technology in medicine: A survey," *J. Elect. Comput. Eng.*, vol. 2012, pp. 3:1–3:9, 2012.
[39] M. M. Lee, E.-M. Lee, B. L. Cho, K. Eshraghian, and Y.-H. Kim, "The UTCOMS: a wireless video capsule nanoendoscope," in *Proc. SPIE*, 2006, vol. 6082, pp. 60 820F–60 820F–10.
[40] E. Karapistoli, D. Stratogiannis, G. Tsiropoulos, and F. Pavlidou, "MAC protocols for ultra-wideband ad hoc and sensor networking: A survey," in *Proc. ICUMT*, St. Petersburg, Russia, 2012, pp. 834–841.

G. Enrico Santagati (S'13) received the B.S. and M.S. degrees in telecommunication engineering from the University of Catania, Catania, Italy, in 2010 and 2012, respectively, and is currently pursuing the Ph.D. degree in electrical engineering at the University at Buffalo, The State University of New York (SUNY), Buffalo, NY, USA.

He is currently working with the Wireless Networks and Embedded Systems Laboratory under the guidance of Prof. Tommaso Melodia. His current research interests are in ultrasonic intrabody networks and software defined radios.

Tommaso Melodia (M'07) received the "Laurea" and Doctorate degrees in telecommunications engineering from the University of Rome "La Sapienza," Rome, Italy, in 2001 and 2005, respectively, and the Ph.D. degree in electrical and computer engineering from the Georgia Institute of Technology, Atlanta, GA, USA, in 2007.

He is an Associate Professor with the Department of Electrical Engineering, University at Buffalo, The State University of New York (SUNY), Buffalo, NY, USA, where he directs the Wireless Networks and Embedded Systems Laboratory. His current research interests are in modeling, optimization, and experimental evaluation of wireless networks, with applications to cognitive and cooperative networking, ultrasonic intrabody networks, multimedia sensor networks, and underwater networks.

Prof. Melodia serves in the editorial boards of the IEEE TRANSACTIONS ON WIRELESS COMMUNICATIONS, IEEE TRANSACTIONS ON MOBILE COMPUTING, IEEE TRANSACTIONS ON MULTIMEDIA, and *Computer Networks*. He received a National Science Foundation CAREER Award. He coauthored a paper that was recognized as the Fast Breaking Paper in the field of Computer Science by Thomson ISI Essential Science Indicators and a paper that received an Elsevier Top Cited Paper Award.

Laura Galluccio (M'02) received the Laurea Degree in electrical engineering and Ph.D. degree in electrical, computer, and telecommunications engineering from the University of Catania, Catania, Italy, in 2001 and 2005, respectively.

In 2002, she was also with the Italian National Consortium of Telecommunications (CNIT), where she worked as a Research Fellow within the Virtual Immersive Communications (VICOM) and the SATNEX Projects. Since 2010, she has been an Assistant Professor with the University of Catania. From May to July 2005, she was a Visiting Scholar with the COMET Group, Columbia University, New York, NY, USA. Her research interests include unconventional communication networks, software defined networks, and network performance analysis.

Dr. Galluccio is a member of the SIGMOBILE and ACM N2Women Group. She serves in the editorial boards of *Ad Hoc Networks* and *Wireless Communications and Mobile Computing*.

Sergio Palazzo (M'92–SM'99) received the degree in electrical engineering from the University of Catania, Catania, Italy, in 1977.

Since 1987, he has been with the University of Catania, where is now a Professor of telecommunications networks. In 1994, he spent the summer with the International Computer Science Institute (ICSI), Berkeley, CA, USA, as a Senior Visitor. His current research interests include mobile systems, wireless and satellite IP networks, and protocols for the next generation of the Internet.

Prof. Palazzo has been serving on the Technical Program Committee of INFOCOM, the IEEE Conference on Computer Communications, since 1992. He has been the General Chair of some ACM conferences, including MobiHoc 2006 and MobiOpp 2010, and currently is a member of the MobiHoc Steering Committee. He has also been the TPC Co-Chair of some other conferences, including IFIP Networking 2011, IWCMC 2013, and European Wireless 2014. He currently serves on the Editorial Board of *Ad Hoc Networks*. In the recent past, he also was an Editor of the *IEEE Wireless Communications Magazine* (formerly *IEEE Personal Communications Magazine*), IEEE/ACM TRANSACTIONS ON NETWORKING, IEEE TRANSACTIONS ON MOBILE COMPUTING, *Computer Networks*, and *Wireless Communications and Mobile Computing*. He is a recipient of the 2003 Visiting Erskine Fellowship by the University of Canterbury, Christchurch, New Zealand.